Enhanced Electron Transport in Epitaxial Annealed Graphene Titanium Dioxide Heterojunction

Nelson Mugambi [1], **James Mbiyu Ngaruiya** [1], **Simon Waweru Mugo** [1]

[1] *Jomo Kenyatta University of Agriculture and Technology*
P. O. Box 62 000 – 00200, Nairobi, Kenya

DOI: 10.22178/pos.92-1

LCC Subject Category: QC1-999

Received 28.04.2023
Accepted 29.05.2023
Published online 31.05.2023

Corresponding Author:
Nelson Mugambi
nelmug2013@gmail.com

Abstract. Titanium dioxide (TiO_2) photocatalyst is a widely acceptable photo catalyst candidate due to its environment friendliness, cost-effectiveness, intrinsic electronics, photostability, good surface properties, and non-toxicity. However, TiO_2 faces significant challenges for commercial exploitations, including high recombination rates, low quantum yield, and low visible light photo conversion efficiency. In this research, the optical properties of graphene TiO_2 heterojunction were evaluated in measurements of Transmittance and Reflectance. Optical parameters in terms of WDD dispersion energy and dielectric constants were studied by annealing the films in the air up to 450 °C at 1 step, 2 °C/min and 1 °C/min annealing rates. Transmittance for the film annealed at 1 °C/min showed the highest transmittance of 86.57% and 74.07% for graphene and graphene TiO_2, respectively. SCOUT software modelled Transmittance data to obtain refractive index. Refractive indices for pristine, 1 step, 2 °C/min, and 1 °C/min TiO_2 films obtained at 550 nm were found to be 0.51, 034, 0.40 and 0.49, respectively. Porosity and dispersion energy for the lowest annealing rates (1 °C/min) was found to be 49 % and 12.7 eV in that order. Real and imaginary Interband transition (2.33–4.04) x 10^{-6} and (0.23–2.73) x 10^{-6} in that order, linear and nonlinear optical susceptibility (1.42–2.18) x 10^{-1} and (4.12–22.50) x 10^{-14}, optical conductivity (2.51–13.2) x 10^{13} and electrical conductivity (3.89–4.60) x 10^{10} were enhanced with decreasing annealing rates. This is due to pole filing, film densification, increased lattice absorption and scattering centres and improved crystallinity of the films due to heat treatment and large-area graphene anchoring. The findings revealed that annealing graphene - TiO_2 passivates its surface, reducing its boundary traps owing to quantum confinement effects and improving the electron transport throughout the heterojunction.

Keywords: graphene; titanium dioxide; annealing rates; transition; heterojunction.

INTRODUCTION

Rising energy demand has dramatically led to rapid development and interest in photovoltaic (PV) technology – progress exploitation towards reduction of cost and improvement of efficiencies of solar cells [1]. TiO_2 draws significant attention among many semiconductors (such as SnO_2, TiO_2, ZnO, CdS, WO3 etc.) due to its high activity, low toxicity, and superchemical stability [2, 3]. In addition, further potential applications are being investigated for sensor devices, electro-optical, micromechanical and photovoltaic [4]. Common polymorphs of TiO_2, naturally occurring, includes; brookite, rutile, or anatase. Anatase nanosized TiO_2 is easily obtained with short diameters of less than 14 nm. Both rutile and anatase absorb the ultraviolet and are transparent in their visible region [5]. The band gap of anatase TiO_2 is 3.18 eV, while that of rutile is 3.08 eV. Both absorb only 5% of sunlight in the UV region, limiting their applications due to their low quantum yield [6].

Two TiO_2 bottlenecks include a lack of visible light response, high charge recombination rates, and short free path of electrons that hinder its applications [7, 8]. Researchers have classified two practical approaches to overcome these shortages: surface sensitization and internal doping [8, 9]. By annealing TiO_2, film morphology, crystallinity, surface porosity, and electrical resistivity are altered [10].

Different approaches to improve the photocatalytic performances of TiO2 have been investigated, including loading with noble metal parti-

cles, use of co-catalysts, metallic or nonmetallic doping and dye [11-13]. The photocatalytic activity of TiO2 enhancement utilizing visible light has been modified to form carbon-TiO_2 using carbonaceous substances such as graphene, fullerenes and carbon nanotubes [14–16]. Graphene is a 2D honeycomb carbon sheet with excellent properties such as zero band gap and prolonged electron mobility (200,000 $cm^2 V^{-1}s^{-1}$). Large specific area (2630 $m^2 g^{-1}$), which acts as absorption sites, excellent electron tank, high visible light transparency, high thermal (≈ 5000 W $m^{-1} K^{-1}$), and high electrical conductivity endow it as a beautiful photo catalyst modifier [17-19]. Transmittance and Reflectance of graphene TiO_2 films were characterized by UV-VIS spectroscopy [20] and optical parameters such as refractive index, extinction coefficient, absorption coefficient, and dielectric constants analysis done by Scout software [21]. The optical properties of TiO_2 were enhanced by shifting the absorption edge toward a longer wavelength once graphene is incorporated to form graphene TiO_2 nanocomposite [22].

In the present work, TiO_2 thin films were coated on graphene on a glass substrate, and the composite was studied holistically. This is to evaluate the influence of annealing and graphene on electron transport and crystallinity of TiO_2 films by exploring dispersion parameters, porosity and dielectric characterization.

Experimental Procedure

Graphene monolayer grown with Roll-to-roll (R2R) chemical vapour deposition (CVD) and wet transfer synthesis on glass substrate were sourced from Charm Graphene CO., limited.

The graphene on the glass was then cleaned gently for about 5 minutes in analytical acetone grade 99.5% purity using cotton swamps, dipped in ethanol, and then rinsed with deionized water for about five minutes. The substrates were then dried by blowing them onto pressurized warm air and stored in a desiccator.

A scotch magic tape was placed on graphene on a glass substrate, leaving a 1 x 1 cm^2 window to control TiO_2 thickness. T/SP, 18% wt, 15-20 nm TiO_2 nanocrystalline, sourced from Solaronix, Switzerland) was coated on the graphene 50 Ω/sq, using a clean tapered glass rod by sol-gel doctor-blading technique [23]. Uniform pressure was applied on the pasted region to obtain the desired film thickness. The films were free for about 20 minutes to enhance homogeneity.

The freshly prepared samples were annealed using KL 420 muffle furnace at 2 and 1 °C/min annealing rates up to 450 °C followed by 30 minutes of sintering to enhance the roughness and crystallinity of the films [24]. A few films were left pristine while others were subjected to 1 step annealing up to 450 °C, left to sinter for about 30 minutes, and then allowed to cool to room temperature.

Optical transmittance was measured using Shimadzu UV VIS Probe 1800 Spectrophotometer at 200–1100 nm. Optical parameters such as refractive index (n), absorption coefficient (α), extinction coefficient (k), real and imaginary dielectric constant ($\varepsilon_1, \varepsilon_2$) were obtained with SCOUT software.

Relative density, Porosity, Dispersion energy, interband transition, Energy losses, linear and nonlinear optical susceptibility, and optical and electrical conductivity were obtained. The data collected was processed using version 8.5 Origin Pro software.

RESULTS AND DISCUSSION

Figure 1 shows the transmittance spectra of annealed graphene samples and graphene TiO_2 composite in the wavelength ranging from 300 to 800 nm.

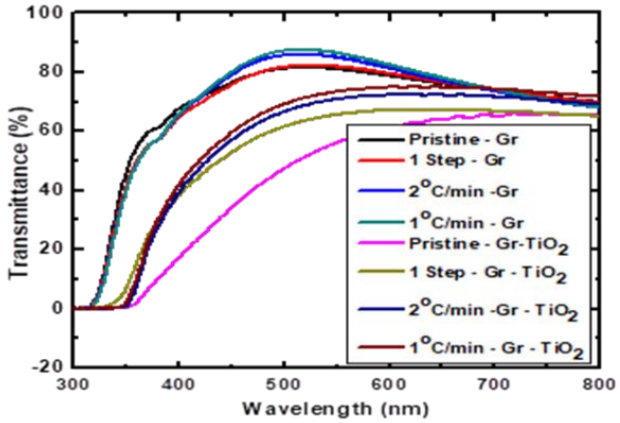

Figure 1 – A graph Transmittance versus Wavelength

The optical transmittance spectra of thermally treated films were found to vary with decreasing annealing rates – a drastic decrease in transmittance in the UV region, which is the ab-

sorption edge. Transmittance enhanced significantly with a reduction in annealing rates with 1 °C per minute, showing the highest transmittance of 86.57 and 74.07 % for graphene and graphene TiO_2, respectively, at 500 nm wavelength. As prepared and annealed, graphene exhibits peaks at 500 nm, whereas graphene – TiO_2 was found at 713.5 nm wavelength. All the films displayed high transmittance within the visible light. It is worth noticing a blue shift in the transmittance of graphene and graphene – TiO_2 films as annealing rates decreased. The graphene monolayer is not expected to change its optoelectronic properties with annealing. Therefore, we report a variation in graphene transmittance at varying annealing rates. This is due to the removal of hydrocarbons and the decrement of wettability and polymer residues. A slight reduction in transmittance with increased annealing rates can be attributed to increased surface roughness or to alleviating oxygen defects [25]. When TiO_2 is annealed at lower annealing rates, oxygen vacancies are formed due to releasing oxygen into the environment. The transmittance values corresponding to $\lambda = 500\ nm$ within the transparent region were recorded in Table 1.

Table 1 – Transmittance and optical parameters of TiO_2 thin films at various annealing rates

Samples	Transmittance, %	Refractive index, n	Relative density, %	Porosity, %
As-Prep	55.71	1.99	51	49
1 Step	65.47	1.67	34	66
2 °C/min	70.55	1.78	40	60
1 °C/min	74.07	1.90	49	51

To obtain the complex optical refractive index, n, of the film, we used relation (1)

$$\tilde{n} = n(w) + ik(w) \quad (1)$$

where the genuine part gives the refractive index n, whereas the imaginary part gives extinction coefficient k, the refractive index values of graphene and graphene TiO_2 films can be obtained from equation (2):

$$n = \left\{ \left[\frac{4R}{(R-1)^2} \right]^{\frac{1}{2}} - \frac{R+1}{R-1} \right\} \quad (2)$$

where R is the reflectance and k is the extinction coefficient [26].

Figure 2 presents plots of the refractive index n, of graphene and graphene TiO_2 films as a function of wavelength.

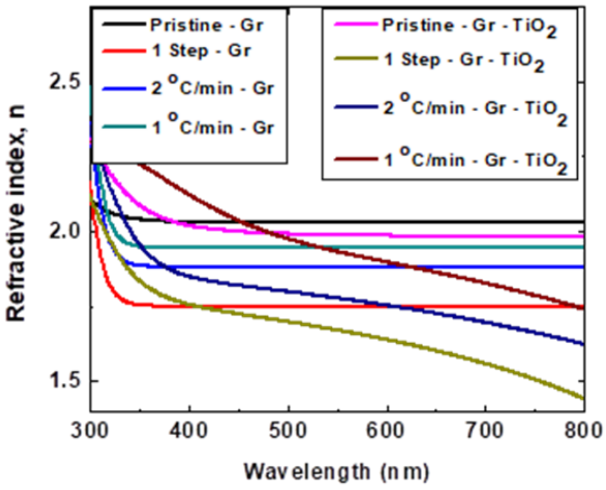

Figure 2 – A graph of refractive index versus wavelength

The refractive index spectra decrease with increasing wavelength revealing a normal dispersion behaviour. However, the refractive index varies with varying annealing rates. For both graphene and graphene TiO_2 films, refractive index spectra increase with decreasing annealing rates, which can be attributed to an increase in packing density and improvement in crystallinity [27]. A decreased refractive index with wavelength can be associated with the resonant effect between irradiated photons and electronic polarization due to film equality between irradiated photons and plasma frequency [27]. The refractive index at $\lambda = 500\ nm$ was recorded in Table 1.

The refractivity of films affects the porosity (the volume of pores per volume) of TiO_2 films. Porosity expressed as a percentage is estimated by the expression (3):

$$Porosity = \left(1 - \frac{{n_p}^2 - 1}{n_0^2 - 1}\right) \times 100 \quad (3)$$

where n_p is the refractivity of the anatase porous films, and n_o =2.52 is the refractivity of bulk TiO_2 [28, 29].

Porosity was obtained using the refractive index within the transparent region corresponding to a wavelength equal to 500 nm, recorded in Table 1. Porosity decreased with decreasing annealing rates, a phenomenon associated with reduced pore size due to film densification and compaction. Therefore, a high refractive index led to the lowest porosity. Film annealed at 1 °C per minute showed the lowest porosity, at 51%. Decreased annealing rates significantly increase TiO2 densely packed particles overlap, reducing porosity. Overlap of particles at low porosity causes an increment in the internal surface area of the material. As porosity decreases, the coordination number (CN) of TiO_2 increases. For densely packed particles with a maximum CN=6, the porosity was found to be 0.41 (41%) [30, 31]. Expression (4), shown below, was used to determine the relative values of films [32].

$$Relative\ density\ = \frac{n^2-1}{n_0^2-1} \times 100 \qquad (4)$$

Figure 3 displays a graph of relative density versus photon energy.

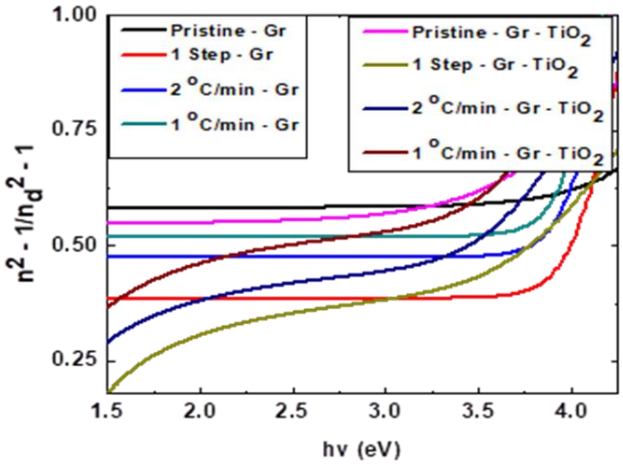

Figure 3 – A graph of refractive index versus annealing rate

The relative density of the annealed films rose with a rise in photon energy. The relative density of the films increased with decreasing annealing rates, which is attributed to the gradual improvement of the quality of the film, film densification, and film crystallization.

Charge transport in a solid-state lattice site is a hopping-like movement that results in electron recombination. Flat, dense TiO_2 electron transfer improves due to better light absorption, pore filing and charge compensation because of a reduction in porosity [33].

A single oscillator model by [34, 35] can examine refractive index dispersion in low absorption regions using the relation (5):

$$(n^2-1)^{-1} = \frac{E_0}{E_d} - \frac{1}{E_0 E_d}(hv)^2 \qquad (5)$$

where E_0 is the single oscillator energy, and E_d is the dispersion energy, h – Planck's constant, v – frequency, hv – photon energy.

Representation spectra of $(n^2\text{-}1)^{-1}$ as a function of $(hv)^2$ for pristine and annealed graphene and graphene TiO_2 films are presented in Figure 4.

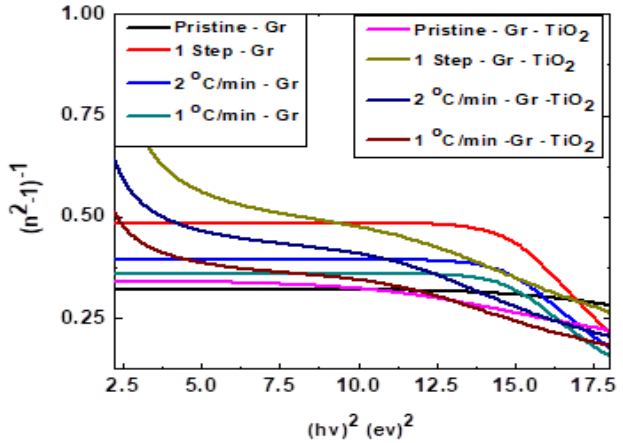

Figure 4 – The plot of $(n^2\text{-}1)^{-1}$ versus $(hv)^2$ of annealed graphene and graphene TiO_2 coatings

$(n^2\text{-}1)^{-1}$ decreases with increasing photon energy. For all the films, $(n^2\text{-}1)^{-1}$ disperses at lower points and clusters together as we approach higher photon energy attributed to the lattice absorption due to impurities and structural defects contained in the inter- crystallite's boundaries containing and increased scattering centres in the films [35].

They fit linearly in Figure 4 and yield straight lines illustrated in Figure 5 ranging from 3.5 to 6.5 $(eV)^2$ chosen from the obtained curvature.

Lattice vibrations contribute negatively to the refractive index, so a positive curvature deviation is observed linearly from long wavelengths [35].

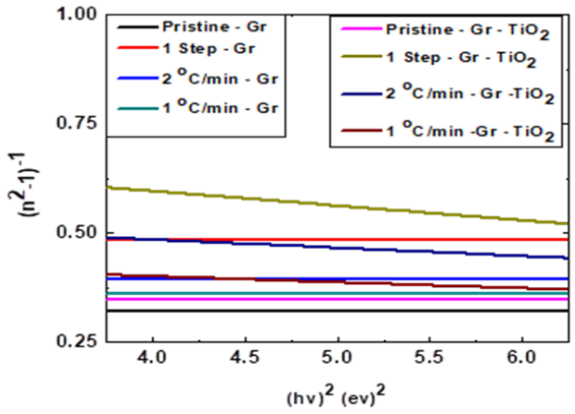

Figure 5 – Linear fit of $(n^2-1)^{-1}$ versus $(hv)^2$ of annealed graphene and graphene TiO_2 coatings

For normal dispersion behaviour, $(E_oE_d)^{-1}$ was obtained from the slope, whereas vertical intercepts yield E_o/E_d from which the oscillator energy, E_o and dispersion energy, E_d were determined. The values for E_o and E_d for pristine and annealed films were tabulated. As seen in Table 2, dispersion energy and oscillator energy increase with decreasing annealing rates at 1 °C per minute.

Table 2 – Dispersions and dielectric parameters of TiO_2 thin films at various annealing rates

Samples	E_d	E_0	Nc	χ^3 x 10^{-13}	χ^1 x 10^{-1}	ε_1	ε_2	Tan δ
As-Prep	45.6	15.8	7.70	30.50	2,35	0.62	0.26	0.41
1 Step	6.38	4.66	1.08	4.12	1.42	0.28	0.03	0.10
2 °C/min	9.77	5.46	1.65	8.70	1.72	0.36	0.13	0.38
1 °C/min	12.7	5.76	2.15	22.50	2.18	0.48	0.32	0.68

This shows the highest values attributed to the film having better excitation energy for electronic transition and appealing strength of interband optical change. High specific surface area and many chemical defects on graphene monolayers make them have high dispersion. This, in return, causes high dispersion when it scaffolders TiO_2 which can probably enhance dye adsorption in DSSC applications.

Dispersion energy, E_d can be related by a relation (6) to determine the coordination number (N_c) [36, 37].

$$E_d = \beta N_c Z_a N_e \quad (6)$$

where β is a covalent or ionic value = 0.37 eV [35] for covalent materials, the formal valence of anion Za=2, and the adequate number of valence electrons per anion Ne, for TiO_2 equals 8.

The particle coordination numbers calculated are displayed in Table 2. These values are seen to increase with decreasing annealing rates. 1 °C per minute achieves a higher particle coordination number attributed to improvement in percolation pathways. For an electron residing on a particular particle, a higher particle coordination number implies that it can percolate in a three-dimensional lattice to another particle.

According to [38], the nonlinear polarizability parameter, also known as nonlinear optical susceptibility χ^3 and the linear optical susceptibility χ^1 can be determined using the Miller rule (7), which is very convenient for visible and near infra-red frequencies.

$$\chi(3) = C\left(\chi^{(1)}\right)^4 = \\ = C\left[\frac{E_oE_d}{4\pi E_o^2-(hv)^2}\right]^4 = \\ = \frac{C}{(4\pi)^4(n^2-1)^4} \quad (7)$$

where C is a constant, $C=10^{-10}$ esu.

Figure 6 displays a graph of the nonlinear optical susceptibility of annealed graphene TiO_2 as a function of photon energy. χ3 spectra increase with increasing photon energy. Linear and nonlinear optical susceptibility was enhanced with decreased annealing rates attributed to the quantum confinement effect. χ3 values were obtained at a corresponding hv = 2.26 eV, and corresponding χ1 values were calculated using equation 7. The values are listed in Table 2.

The lowest annealing (1 °C per minute) exhibited a much higher nonlinear optical susceptibility due to the enhanced crystallinity of TiO_2 on graphene through the possible existence of C-O-Ti bonds associated with facile charge separation [39].

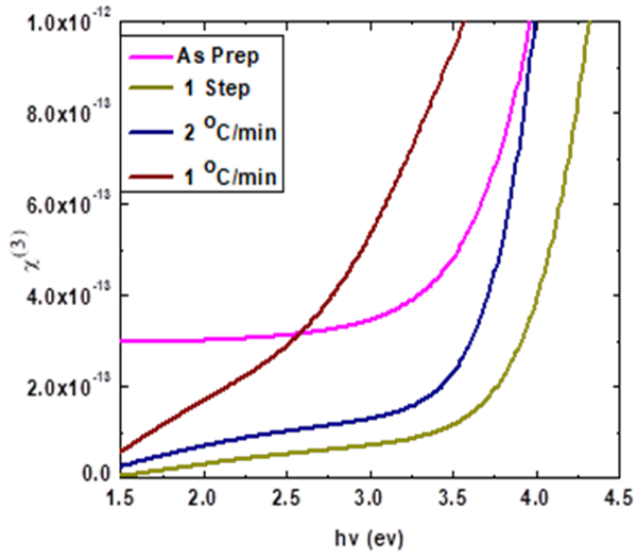

Figure 6 – A graph of nonlinear optical susceptibility of annealed Graphene – TiO_2

The complex refractive index (1) contributes to the dielectric function $\varepsilon = \varepsilon_1 + i\varepsilon_2$ [40] generates real ε_1 and imaginary ε_2 parts of the dielectric constant given by equations (8)-(9).

$$\varepsilon_1 = n^2 - k^2 \quad (8)$$

$$\varepsilon_2 = 2nk \quad (9)$$

Both natural and imaginary parts variations for all graphene TiO_2 films (pristine and annealed) as a function of wavelength are presented in Figure 7.

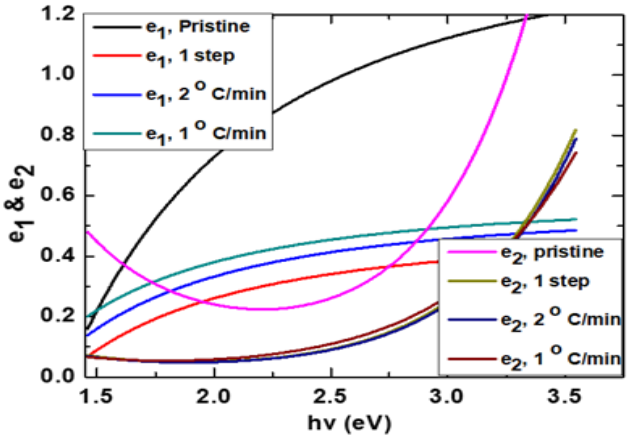

Figure 7 – A variation of real and imaginary parts of pristine and annealed Graphene – TiO_2

ε_1 is higher than ε_2 where ε_1 relates the slowing down of light in the medium, and ε_2 correlates the interaction of matter with the electric field vector, causing the absorption of light. ε_1 and ε_2 increase with increasing photon energy. They are both enhanced with decreasing annealing rates associated with improving the crystallinity of TiO_2 films. These values obtained at hv equal to 2.26 eV are displayed in Table 2.

The variation observed on the real and imaginary parts indicates some interaction between photons and electrons produced in that range [41]. The ratio of the fundamental part of the dielectric constant to that of the imaginary part is more significant than one revealing a clear and visual response of graphene TiO_2 films to the incident radiation falling on its surface. Relation (10) gives the loss tangent, which provides information about the loss factor [42]. Tan δ tabulated in Table 2 is less than one for all the films revealing that the dissipation energy of the movie is relatively low. Lower loss tangents of the films can be associated with favourable optical qualities due to the low scattering of irradiated photons [43].

$$\tan\delta = \frac{\varepsilon_2}{\epsilon_1} \quad (10)$$

Complex interband can be generated from the real and imaginary part of the dielectric constant using relation (11):

$$J_{cv} = J_{cv1} + J_{cv2} = \frac{{m_o}^2 4\pi^2}{e^2 h^2} \frac{(hv)^2}{2} (\varepsilon_1 + i\varepsilon_2) \quad (11)$$

where h is the Plank's constant, e is the electron charge; m_o is the mass of an electron.

Dielectric transition strength is proportional to the genuine part interband transition J_{cv1} and imaginary part interband transition [44].

Pre multiplier $\frac{{m_o}^2 4\pi^2}{e^2 h^2}$ is used as 8.289x

x10^{-6} gcm^{-3}(ev)$^{-2}$ for convenience computation. The dependence of J_{cv1} and J_{cv2} on the photon energy is displayed in Figure 8a. Interband transition strength increases with photon energy. J_{cv} shows enhancement with decreasing annealing rates associated with improved electronic transition probability.

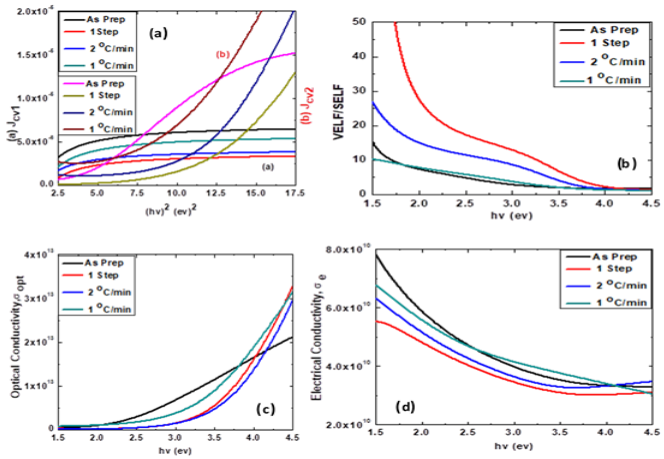

Figure 8 – a) Interband transition verses hv^2, b) Velf/Self , c) optical conductivity, d) electrical conductivity as a function of photon energy

There is a significant increase in J_{cv} at $(hv)^2 > 5.0$ $(eV)^2$, which implies high absorption elevating the excitation of the electrons. This enables electron movements from the valence band to the conduction band. A Greater Jcv ratio of 1 °C per minute reveals low dielectric loss of graphene TiO_2 annealed at the lowest annealing rate, demonstrating an increase in electron density of the film associated with a reduction in charges recombination.

Surface energy loss function (SELF) and volume energy loss (VELF) expresses the energy transferred to and from the topmost atom layer of a compound semiconductor due to electrons' excitation in the surface and bulk. Relations (12) and (13) respectively evaluated both SELF and VELF losses [45].

$$S_{elf} = \left\{-\frac{1}{\varepsilon}\right\} = \frac{\epsilon_2}{(1+\epsilon_1)^2+\epsilon_2^2} \quad (12)$$

$$V_{el} = \left\{-\frac{1}{1+\varepsilon}\right\} = \frac{\epsilon_2}{\epsilon_1^2+\epsilon_2^2} \quad (13)$$

Figure 8b displays the dependence of photon energy and effective VELF/SELF ratio in the visible and ultraviolet regions of graphene TiO_2 pristine and annealed films. Practical VELF/SELF decreased with increasing photon energy Self and Velf values corresponding to values of ε_1 and ε_2 at hv = 2.26 eV are presented in Table 2. SELF and VELF values corresponding to ε_1 and ε_2 at hv = 2.26 eV are shown in Table 2. Volume energy losses are higher than surface energy losses, implying that an electron dissipates more energy as it traverses through the bulk than the surface. SELF and VELF increase with decreasing annealing rates, showing nearly identical behaviour as free charge carriers travel through the surface and size. Similarly, VELF/SELF decreased with decreasing annealing rates, indicating an improvement in the crystallinity of films due to increased surface mobility of adatoms on the surface of the glass substrate and a favourable anchor of TiO_2 on graphene. The earlier report shows that more energy is lost when a fast-moving electron passes through bulk than the surface of a medium due to the excitation of plasma oscillation of the electron [43, 46, 47].

Scattering energy losses and total absorption mainly affect a medium's absorption coefficient (α). Absorption coefficient values were obtained from scout software by simulating transmittance data. The absorption coefficient of graphene TiO_2 decreased with increasing wavelength. A low absorption coefficient at a high wavelength implies a low possibility of electron transition since the photon energy was insufficient to move the electron from the valence band to the conduction band of a semiconductor. There is a higher possibility for electron transition at a shorter wavelength since the photon energy is enough. The probability of an electron transition is higher where the values of α are > 10^4 cm^{-1}. At α < 10^4 cm^{-1}, electron transition is indirect; therefore, the phonon maintains the electron momentum [48]. Values for α at λ = 500 nm within the transparent region were listed in Table 3.

Table 3 – Electron transition and transport parameter of graphene TiO_2 thin films at various annealing rates

Samples	J_{cv1} x 10^{-6}	J_{cv2} x 10^{-6}	Self	Velf	Velf / Self	α x 10^3	σ_{opt} x 10^{13}	σ_e x 10^{10}
As-Prep	5.13	2.13	0.10	0.57	5.98	36.55	17.34	4.57
1 Step	2.33	0.23	0.02	0.35	20.64	5.92	2.51	3.89
2 °C/min	2.95	1.11	0.07	0.93	12.85	6.99	2.79	4.13
1 °C/min	4.04	2.73	0.14	0.95	6.75	28.58	13.20	4.60

α increased with decreasing annealing rates with 1 °C per minute, showing the highest α, implying a higher probability of electron transition due to closeness in the top points of a valence band and bottommost moments of the

conduction band.

The optical conductivity (σ_{opt}), electrical conductivity (σ_{e}) and absorption coefficient are related by equations (14)-(15) in that order [42].

$$\sigma_{opt} = \frac{\alpha nc}{4\pi} \quad (14)$$

$$\sigma_{opt} = \frac{\alpha nc}{4\pi} \quad (15)$$

where n is the refractive index and c is the velocity of the radiation.

The diversity of σ_{opt} for pristine and annealed graphene TiO_2 films as a function of photon energy is represented in Figure 8c. It is seen from the figure that σ_{opt} increases with the photon energy, which we attribute to the photon energy exciting the electrons. The optical conductivity of graphene TiO_2 was elevated with decreasing annealing rates attributed to TiO_{1-x} oxygen deficit acting as donor defects due to oxygen vacancies and interstitial titanium states [49]. Maximum conductivity is experienced at one °C per minute, a phenomenon of the effect of oxygen vacancies on the film's carrier density [50]. Figure 8d illustrates the dependence of electrical conductivity as a function of photon energy. It is noteworthy that σ_{e} is significantly reduced with increased photon energy due to electrons trapping at the defect centres. Electrical conductivity increases with decreased annealing rates, which can be attributed to crystallinity and lattice absorption improvement.

Porosity, nonlinear susceptibility and optical conductivity correlation have been presented in Figure 9. Nonlinear susceptibility and visual conductivity increase with decreasing annealing rates. Moreover, porosity decreased with lowering annealing rates due to gradual quality improvement in film crystallization, film pore filing and densification due to the local migration of matter attributed to particle diffusive sintering.

Authors [51] found higher values of porosity for TiO_2 film anchored on FTO than the values we find of TiO_2 on graphene due to the large surface area of graphene that offer a scaffold anchor of TiO_2. Tiny gaps and voids at the FTO/TiO_2 interface cause higher porosity due to the uneven microstructure of FTO glass. According to [52], annealing time and temperature influence the porosity aggregate and quality of the films.

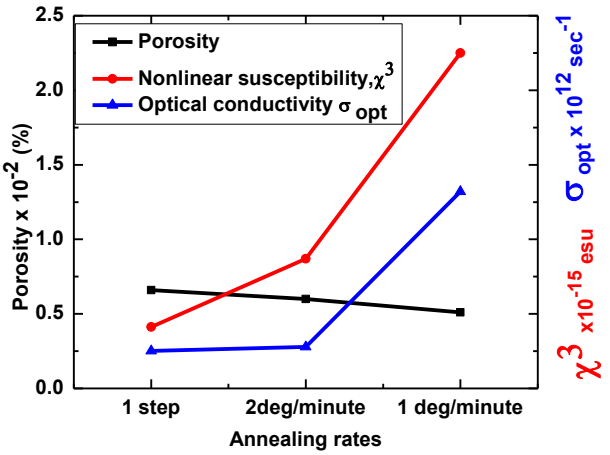

Figure 9 – Correlation of Porosity, nonlinear susceptibility and optical conductivity of annealed graphene TiO_2 films

Graphene TiO_2 film's significant nonlinear susceptibility of order 10^{-14} esu is attributed to the substantial enhancement of the local field. Nonlinear optical exposure increased with decreasing annealing rates attributed to the lattice's vibration and dispersion effects due to grain size increase as the film transited from amorphous to crystalline. We associate the increase in S_{EL}/V_{EL} with improving the crystalline quality of the TiO_2 films. The surface-to-volume ratio has the same trend as dispersion energy.

CONCLUSIONS

A UV VIS spectrophotometer has characterized graphene TiO2 films prepared by Doctor Blade. Graphene and graphene TiO2 have obtained in the range 300–800 nm, from which refractive index, relative density, porosity, dispersion, linear and nonlinear susceptibility, interband transition, energy losses, optical and electrical conductivity optical parameters were deducted. Graphene metal being a semimetal not expected to vary optoelectronic properties by annealing. A transmittance, porosity and dispersion parameters variation at different annealing rates was reported. This variation can be attributed to removing hydrocarbons, wettability decrement, and polymer residues. All the films exhibit high transmittance

(~ 80– 86% for graphene) and (~ 56– 74% for graphene TiO_2), decreasing porosity (66- 49%), sizeable third-order susceptibility (4.12–30.50) x 10^{-14} esu. Interband transition increased with decreasing annealing rates showing a higher probability of an electron transit from the valence band to the conduction band. The experimental results reveal the film for graphene TiO_2 annealed at 1 °C per minute is suitable for application in optoelectronic owing to its low porosity, significant third-order susceptibility, higher interband transition, low VELF/SELF-ratio, higher optical and electrical conductivity and good crystallinity.

Therefore, we have successfully evaluated the influence of anchoring TiO_2 on graphene and annealing temperature. The films annealed at 1 °C/min rate showed better diffusion rate, longer electron lifetime due to low recombination rate, and improved crystallinity that enhanced electron transport of the films.

REFERENCES

1. Serrano, E., Rus, G., & García-Martínez, J. (2009). Nanotechnology for sustainable energy. *Renewable and Sustainable Energy Reviews, 13*(9), 2373–2384. doi: 10.1016/j.rser.2009.06.003
2. Drunka, R., Grabis, J., Jankovica, D., Krumina, A., & Rasmane, D. (2015). Microwave-assisted synthesis and photocatalytic properties of sulphur and platinum modified TiO2nanofibers. *IOP Conference Series: Materials Science and Engineering, 77*, 012010. doi: 10.1088/1757-899x/77/1/012010
3. Wang, S., Pan, L., Song, J.-J., Mi, W., Zou, J.-J., Wang, L., & Zhang, X. (2015). Titanium-Defected Undoped Anatase TiO2 with p-Type Conductivity, Room-Temperature Ferromagnetism, and Remarkable Photocatalytic Performance. *Journal of the American Chemical Society, 137*(8), 2975–2983. doi: 10.1021/ja512047k
4. Singh, R. (2004). Nano-structured CdTe, CdS and TiO2 for thin film solar cell applications. *Solar Energy Materials and Solar Cells, 82*(1–2), 315–330. doi: 10.1016/j.solmat.2004.02.006
5. Zallen, R., & Moret, M. P. (2006). The optical absorption edge of brookite TiO2. *Solid State Communications, 137*(3), 154–157. doi: 10.1016/j.ssc.2005.10.024
6. Matthews, R. W. (1987). Photooxidation of organic impurities in water using thin films of titanium dioxide. *The Journal of Physical Chemistry, 91*(12), 3328–3333. doi: 10.1021/j100296a044
7. Asahi, R., Morikawa, T., Ohwaki, T., Aoki, K., & Taga, Y. (2001). Visible-Light Photocatalysis in Nitrogen-Doped Titanium Oxides. *Science, 293*(5528), 269–271. doi: 10.1126/science.1061051
8. Hu, G., & Tang, B. (2013). Photocatalytic mechanism of graphene/titanate nanotubes photocatalyst under visible-light irradiation. *Materials Chemistry and Physics, 138*(2–3), 608–614. doi: 10.1016/j.matchemphys.2012.12.027
9. Qianqian, Z., Tang, B., & Guoxin, H. (2011). High photoactive and visible-light responsive graphene/titanate nanotubes photocatalysts: Preparation and characterization. *Journal of Hazardous Materials, 198*, 78–86. doi: 10.1016/j.jhazmat.2011.10.012
10. Hasan, M. M., Haseeb, A. S. M. A., Saidur, R., Masjuki, H. H., & Hamdi, M. (2009). Synthesis and Annealing of Nanostructured TiO2 Films by Radio-Frequency Magnetron Sputtering. *Journal of Applied Sciences, 9*(15), 2815–2821. doi: 10.3923/jas.2009.2815.2821
11. Gu, Y., Xing, M., & Zhang, J. (2014). Synthesis and photocatalytic activity of graphene based doped TiO2 nanocomposites. *Applied Surface Science, 319*, 8–15. doi: 10.1016/j.apsusc.2014.04.182
12. Cai, J., Wu, X., Li, S., & Zheng, F. (2017). Controllable location of Au nanoparticles as cocatalyst onto TiO2@CeO2 nanocomposite hollow spheres for enhancing photocatalytic activity. *Applied Catalysis B: Environmental, 201*, 12–21. doi: 10.1016/j.apcatb.2016.08.003
13. Cheng, L., Qiu, S., Chen, J., Shao, J., & Cao, S. (2017). A practical pathway for the preparation of Fe2O3 decorated TiO2 photocatalyst with enhanced visible-light photoactivity. *Materials Chemistry and Physics, 190*, 53–61. doi: 10.1016/j.matchemphys.2017.01.001

14. Qi, K., Selvaraj, R., Al Fahdi, T., Al-Kindy, S., Kim, Y., Wang, G.-C., Tai, C.-W., & Sillanpää, M. (2016). Enhanced photocatalytic activity of anatase-TiO2 nanoparticles by fullerene modification: A theoretical and experimental study. *Applied Surface Science, 387*, 750–758. doi: 10.1016/j.apsusc.2016.06.134

15. Qin, X., He, F., Chen, L., Meng, Y., Liu, J., Zhao, N., & Huang, Y. (2016). Oxygen-vacancy modified TiO2 nanoparticles as enhanced visible-light driven photocatalysts by wrapping and chemically bonding with graphite-like carbon. *RSC Advances, 6*(13), 10887–10894. doi: 10.1039/c5ra27209b

16. Rahbar, M., & Behpour, M. (2016). Multi-walled carbon nanotubes/TiO2 thin layer for photocatalytic degradation of organic pollutant under visible light irradiation. *Journal of Materials Science: Materials in Electronics, 27*(8), 8348–8355. doi: 10.1007/s10854-016-4845-2

17. Tang, B., Chen, H., Peng, H., Wang, Z., & Huang, W. (2018). Graphene Modified TiO2 Composite Photocatalysts: Mechanism, Progress and Perspective. *Nanomaterials, 8*(2), 105. doi: 10.3390/nano8020105

18. Novoselov, K. S., Geim, A. K., Morozov, S. V., Jiang, D., Katsnelson, M. I., Grigorieva, I. V., Dubonos, S. V., & Firsov, A. A. (2005). Two-dimensional gas of massless Dirac fermions in graphene. *Nature, 438*(7065), 197–200. doi: 10.1038/nature04233

19. Balandin, A. A., Ghosh, S., Bao, W., Calizo, I., Teweldebrhan, D., Miao, F., & Lau, C. N. (2008). Superior Thermal Conductivity of Single-Layer Graphene. *Nano Letters, 8*(3), 902–907. doi: 10.1021/nl0731872

20. Balandin, A. A., Ghosh, S., Bao, W., Calizo, I., Teweldebrhan, D., Miao, F., & Lau, C. N. (2008). Superior Thermal Conductivity of Single-Layer Graphene. *Nano Letters, 8*(3), 902–907. doi: 10.1021/nl0731872

21. WTheiss Hardware and Software. (2023). Scout. Retrieved from https://wtheiss.com/wordpress/?cat=4

22. Kazmi, S. A., Hameed, S., Ahmed, A. S., Arshad, Mohd., & Azam, A. (2017). Electrical and optical properties of graphene-TiO2 nanocomposite and its applications in dye sensitized solar cells (DSSC). *Journal of Alloys and Compounds, 691*, 659–665. doi: 10.1016/j.jallcom.2016.08.319

23. Frederichi, D., Scaliante, M. H. N. O., & Bergamasco, R. (2020). Structured photocatalytic systems: photocatalytic coatings on low-cost structures for treatment of water contaminated with micropollutants—a short review. *Environmental Science and Pollution Research, 28*(19), 23610–23633. doi: 10.1007/s11356-020-10022-9

24. John, B. M. , Mugo, S. W. , & Ngaruiya, J. M. (2018). Effect of Annealing Rates on Surface Roughness of TiO_2 Thin films. *Journal of Materials Physics and Chemistry*, *6*(2), 43-46.

25. Gupta, V., & Mansingh, A. (1996). Influence of postdeposition annealing on the structural and optical properties of sputtered zinc oxide film. *Journal of Applied Physics, 80*(2), 1063–1073. doi: 10.1063/1.362842

26. Abeles, F. (1972). *Optical Properties of Solids*. London: North-Holland Publishing Company.

27. Hassanien, A. S., & Akl, A. A. (2018). Optical characteristics of iron oxide thin films prepared by spray pyrolysis technique at different substrate temperatures. *Applied Physics A, 124*(11). doi: 10.1007/s00339-018-2180-6

28. Ye, Q., Liu, P. Y., Tang, Z. F., & Zhai, L. (2007). Hydrophilic properties of nano-TiO2 thin films deposited by RF magnetron sputtering. *Vacuum, 81*(5), 627–631. doi: 10.1016/j.vacuum.2006.09.001

29. Liu, J., Gan, D., Hu, C., Kiene, M., Ho, P. S., Volksen, W., & Miller, R. D. (2002). Porosity effect on the dielectric constant and thermomechanical properties of organosilicate films. *Applied Physics Letters, 81*(22), 4180–4182. doi: 10.1063/1.1525054

30. Bouvard, D., & Lange, F. F. (1992). Correlation between random dense parking and random dense packing for determining particle coordination number in binary systems. *Physical Review A, 45*(8), 5690–5693. doi: 10.1103/physreva.45.5690

31. Ni, M., Leung, M. K. H., Leung, D. Y. C., & Sumathy, K. (2006). An analytical study of the porosity effect on dye-sensitized solar cell performance. *Solar Energy Materials and Solar Cells, 90*(9), 1331–1344. doi: 10.1016/j.solmat.2005.08.006

32. Ohyama, M., Kouzuka, H., & Yoko, T. (1997). Sol-gel preparation of ZnO films with extremely preferred orientation along (002) plane from zinc acetate solution. *Thin Solid Films, 306*(1), 78–85. doi: 10.1016/s0040-6090(97)00231-9

33. Smestad, G. P., Spiekermann, S., Kowalik, J., Grant, C. D., Schwartzberg, A. M., Zhang, J., Tolbert, L. M., & Moons, E. (2003). A technique to compare polythiophene solid-state dye sensitized TiO2 solar cells to liquid junction devices. *Solar Energy Materials and Solar Cells, 76*(1), 85–105. doi: 10.1016/s0927-0248(02)00252-0

34. Wemple, S. H., & DiDomenico, M. (1969). Oxygen-Octahedra Ferroelectrics. II. Electro-optical and Nonlinear-Optical Device Applications. *Journal of Applied Physics, 40*(2), 735–752. doi: 10.1063/1.1657459

35. Wemple, S. H., & DiDomenico, M. (1971). Behavior of the Electronic Dielectric Constant in Covalent and Ionic Materials. *Physical Review B, 3*(4), 1338–1351. doi: 10.1103/physrevb.3.1338

36. Tan, W. C., Koughia, K., Singh, J., & Kasap, S. O. (2006). Fundamental Optical Properties of Materials I. Optical Properties of Condensed Matter and Applications, 1–25. doi: 10.1002/0470021942.ch1

37. Márquez, E., Ramírez-malo, J. B., Villares, P., Jiménez-Garay, R., & Swanepoel, R. (1995). Optical characterization of wedge-shaped thin films of amorphous arsenic trisulphide based only on their shrunk transmission spectra. *Thin Solid Films, 254*(1–2), 83–91. doi: 10.1016/0040-6090(94)06267-o

38. Wagner, S. J., Meier, J., Helmy, A., Stewart, A., Sorel, M., & Hutchings, D. (2007). Polarization-dependent nonlinear refraction and two-photon absorption in GaAs/AlAs superlattice waveguides below the half-bandgap. *Journal of the Optical Society of America B, 24*, 1557-1563.

39. Hassanien, A. S., Sharma, I., & Akl, A. A. (2020). Physical and optical properties of a-Ge-Sb-Se-Te bulk and film samples: Refractive index and its association with electronic polarizability of thermally evaporated a-Ge15-xSbxSe50Te35 thin-films. *Journal of Non-Crystalline Solids, 531*, 119853. doi: 10.1016/j.jnoncrysol.2019.119853

40. Spicer, W. E. (1972). Introduction. In F. Abeles (Ed.)*, Optical Properties of Solids*. London: North-Holland Publishing Company.

41. Chander, S., & Dhaka, M. S. (2016). Thermal evolution of physical properties of vacuum evaporated polycrystalline CdTe thin films for solar cells. *Journal of Materials Science: Materials in Electronics, 27*(11), 11961–11973. doi: 10.1007/s10854-016-5343-2

42. Astinchap, B., Moradian, R., & Gholami, K. (2017). Effect of sputtering power on optical properties of prepared TiO 2 thin films by thermal oxidation of sputtered Ti layers. *Materials Science in Semiconductor Processing, 63*, 169–175. doi: 10.1016/j.mssp.2017.02.007

43. Yang, C., Fan, H., Xi, Y., Chen, J., & Li, Z. (2008). Effects of depositing temperatures on structure and optical properties of TiO2 film deposited by ion beam assisted electron beam evaporation. *Applied Surface Science, 254*(9), 2685–2689. doi: 10.1016/j.apsusc.2007.10.006

44. Loughin, S., French, R. H., Noyer, L. K. D., Ching, W.-Y., & Xu, Y.-N. (1996). Critical point analysis of the interband transition strength of electrons. *Journal of Physics D: Applied Physics, 29*(7), 1740–1750. doi: 10.1088/0022-3727/29/7/009

45. Al-Mudhaffer, M. F., Nattiq, M. A., Jaber, M. A. (2012). Linear optical properties and energy loss function of Novolac: Epoxy blend film. *Archive Applied Science Research,* 4(4), 1731–1740.

46. Yakuphanoglu, F., Cukurovali, A., & Yilmaz, İ. (2004). Single-oscillator model and determination of optical constants of some optical thin film materials. *Physica B: Condensed Matter, 353*(3–4), 210–216. doi: 10.1016/j.physb.2004.09.097

47. Sarkar, S., Garain, S., Mandal, D., & Chattopadhyay, K. K. (2014). Electro-active phase formation in PVDF–BiVO4 flexible nanocomposite films for high energy density storage application. *RSC Adv., 4*(89), 48220–48227. doi: 10.1039/c4ra08427f

48. Crane, M., & Hassan, Y. (1989). *Solar Cells* (Collage of Education, University of Mosul). N. d.

49. Nowotny, J., Sorrell, C. C., Bak, T., & Sheppard, L. R. (2005). Defect disorder, transport and photoelectrochemical properties of TiO 2. *Materials for Energy Conversion Devices*, 84–119. doi: 10.1533/9781845690915.1.84

50. Yakuphanoglu, F., Cukurovali, A., & Yilmaz, İ. (2005). Refractive index and optical absorption properties of the complexes of a cyclobutane containing thiazolyl hydrazone ligand. Optical *Materials, 27*(8), 1363–1368. doi: 10.1016/j.optmat.2004.09.021

51. Mugambi, N., Mbiyu Ngaruiya, J., Waweru Mugo, S., Gitonga Riungu, G., & Mbae John, G. (2021). Influence of Post Annealing Rates on Porosity, Dispersion Energy and Associated Dielectric Energy Losses of TiO_2 Thin Films. *Journal of Photonic Materials and Technology, 7*(1), 1. doi: 10.11648/j.jmpt.20210701.11

52. Aljufairi, N. H. (2012). Electric properties and surface structure of TiO_2 for solar cells. *Energy, 39*(1), 6–10. doi: 10.1016/j.energy.2011.08.057